Chemical Engineering Journal 519 (2025) 165613

Contents lists available at ScienceDirect

Chemical Engineering Journal

journal homepage: www.elsevier.com/locate/cej

Intrinsic nanoconfinement design in halloysite nanotubes enhances the affinity of zirconium phosphate for efficient removal of heavy metal ions

Rong Yang [a], Di Meng [a], Xinyao Zhang [b], Weixuan Zhao [b], Xuanjie Huang [a], Zulin Wang [b], Bo Ma [c], Jun Yao [c], Wenjihao Hu [b,*]

[a] School of Metallurgy and Environment, Central South University, Changsha 410083, China
[b] School of Minerals Processing and Bioengineering, Central South University, Changsha 410083, China
[c] School of Water Resources and Environment, Research Center of Environmental Science and Engineering, China University of Geosciences (Beijing), Beijing 100083, China

ARTICLE INFO

Keywords:
Nanoconfined structure
Halloysite nanotubes
Zirconium phosphate
Adsorption
Atomic force microscopy (AFM)

ABSTRACT

Confining the active adsorption materials within the nanostructure space can significantly improve adsorption performance. However, the fundamental mechanisms by which intrinsic nanoconfinement in clay minerals modulates the microstructure of active materials and regulates interfacial interactions remain unclear. In this work, a comprehensive analysis was conducted to compare the adsorption performance of two structures: a nonconfined structure (ZrP/HNTs), where zirconium phosphate (ZrP) nanocrystals are grown on the outer surface of halloysite nanotubes (HNTs), and a nanoconfined structure (ZrP@HNTs), where ZrP nanocrystals are confined within HNTs' lumen. The resulting ZrP@HNTs adsorption capacity for Pb (II) was 3 times that of ZrP/HNTs (163.7 vs. 54.6 mg/g), and the adsorption rate increased by 2.8 times. Additionally, the confined structure endowed ZrP@HNTs with remarkable stability, only 6.7% capacity decrease after five cycles. Furthermore, finite element simulations revealed that the nanoconfined structure of ZrP@HNTs effectively enriches Pb(II), increasing its concentration and facilitating adsorption. According to the above result, low and high Pb(II) concentrations were used to simulate the adsorption environments of ZrP/HNTs and ZrP@HNTs, respectively, with atomic force microscopy (AFM) providing key quantitative insights. AFM force spectroscopy further confirmed that the nanoconfined structure enhanced the adhesion energy between Pb(II) and phosphate groups on the ZrP surface from 4.34 $mJ{\cdot}m^{-2}$ to 10.81 $mJ{\cdot}m^{-2}$, directly contributing to improved adsorption stability. These findings offer valuable insights into the role of nanoconfinement in enhancing adsorption efficiency, providing a basis for the development of advanced heavy metal removal technologies.

1. Introduction

The escalating heavy metal pollution crisis urgently demands the development of novel adsorbents to overcome the limitations of traditional materials, such as the environmental susceptibility of activated carbon [1] and the aggregation tendency of nano-iron oxide [2]. To address these challenges, nanoconfinement, achieved by encapsulating active adsorption materials within nanostructured space, has emerged as a promising strategy [3–8]. This strategy in adsorption has garnered significant attention due to the ability to modulate the intrinsic properties of adsorption systems, e.g., material size, phase transition behavior, electronic state, and adsorption capacity [9,10]. For example, when the nanoconfinement channel size was reduced from 200 nm to 20 nm, the proportion of goethite phase in the aging product of iron hydride decreased significantly from 41% to 0%, indicating that the nanoconfinement significantly slows down the phase transition kinetics, allowing iron hydride to maintain its specific adsorption capacity for As (V) after aging for 20 days [11]. Similarly, the α-Fe_2O_3 (~3.9 nm) confined in the mesoporous molecular sieve (MCM-41) channel modulates the electron distribution of Fe(III) from a high-spin state to a low-spin state, thereby significantly improving its adsorption performance to anionic pollutants, making its maximum adsorption capacity for rose red >8 times higher than that of commercial activated carbon [8]. Therefore, the rational design of nanoconfined environments to tailor the intrinsic properties of adsorbents is a critical strategy for achieving superior adsorption performance.

* Corresponding author.
E-mail address: huwenjihaoluke@csu.edu.cn (W. Hu).

https://doi.org/10.1016/j.cej.2025.165613
Received 5 May 2025; Received in revised form 16 June 2025; Accepted 2 July 2025
Available online 4 July 2025

While diverse nanostructures (e.g., porous frameworks [12] and layered materials [13]) have been explored for nanoconfinement, tubular nanomaterials stand out as particularly promising candidates due to their unique structural advantages. Tubular nanomaterials inherent hollow architectures not only provide abundant accessible surface sites with highly unsaturated coordination environments [6,14], but also enable directional transport of molecules and promote their enrichment within the confined space, significantly enhancing adsorption reaction performance [15–17]. In addition, theoretical calculations show that concave surfaces are more conducive to efficient adsorption than convex surfaces [16,18,19]. Therefore, by introducing active centers inside the nanotubes to construct a core-shell adsorbent with a confinement effect, it not only improves the dispersion of the active sites, but also exerts the enrichment effect of the nanotubes on small molecules or ions, thereby preparing materials with excellent adsorption properties. However, current studies predominantly focus on artificially synthesized materials such as carbon nanotubes and mesoporous hexagonal silicates, while the exploration of naturally abundant and cost-effective natural clay nanotubes for nanoconfinement adsorption remain limited [3,20,21].

Halloysite nanotubes (HNTs) are natural clay materials formed by inward coiling of kaolin sheets. HNTs have a unique hollow tubular structure and exhibit different chemical properties on the inner and outer surfaces (Si-O-Si on the outer surface and Al-OH on the inner surface), providing a platform for constructing nanoconfined environments [22–24]. This unique structural feature endows HNTs with a pronounced nanoconfinement effect, enabling precise control over the size, morphology, dispersion, and activity of metals and their compounds grown within the lumen. Notably, this confinement effect is closely correlated with the catalytic efficiency, adsorption capacity, and chemical reactivity of the material [25,26], offering a valuable strategy for optimizing the properties of nanomaterials. Zirconium phosphate (ZrP) is widely used to adsorb heavy metals, radioactive elements and rare earth elements due to its superior ion exchange capacity [7,27,28]. However, its easy agglomeration, difficult recovery and poor adsorption selectivity limit its performance in practical applications [29]. Recent studies have shown that the composite of ZrP and HNTs can effectively improve material properties [30–32]. However, existing studies have mostly focused on surface composites or macroscopic assembly structures, and have not yet systematically explored the regulatory mechanism of HNTs nanoconfined space on ZrP crystal growth and its influence on adsorption properties.

In this work, a confined structure was constructed by spatially restricting the growth of ZrP nanocrystals within the lumen of halloysite nanotubes (HNTs), forming a nanoconfined structure (ZrP@HNTs). For comparison, ZrP nanocrystals grown on the outer surface of HNTs (ZrP/HNTs) were used as the nonconfined control. Confinement within the nanostructured space effectively regulated the growth of ZrP, leading to reduced particle size (4.9 vs. 9.5 nm), enhanced dispersion, and increased exposure of active sites, which are beneficial for the adsorption of Pb(II). Experimental results showed that the maximum adsorption capacity of ZrP@HNTs for Pb(II) was 163.7 mg/g, which is about 3 times that of the ZrP/HNTs. In the presence of high concentrations of competing ions, the adsorption performance of ZrP@HNTs for Pb(II) only decreased by 7.6%, while that of ZrP/HNTs decreased by 32.1%. Furthermore, finite element simulations and atomic force microscopy (AFM) were employed to visualize and quantify the contribution of the nanoconfinement effect within HNTs to the adsorption process. This work demonstrated that nanoconfinement significantly enhances heavy metal adsorption performance by simultaneously optimizing the adsorbent nanostructure and interfacial interaction. In summary, this study enhances the understanding of the nanoconfinement effect and offers theoretical insights and technical guidance for its expanded application in water treatment.

2. Materials and methods

2.1. Materials

Halloysite nanotubes were obtained from Guangzhou Runwo Materials Technology Co., Ltd. Zirconium oxychloride ($ZrOCl_2{\cdot}8(H_2O)$, 99.9%), Calcium nitrate (94%), and phosphoric acid were purchased from Shanghai Macklin Biochemical Co., Ltd., China. Lead nitrate (99%) and 11-mercaptoundecylphosphoric acid (≥90%) were acquired from Aladdin Biochemical Technology Co., Ltd. in Shanghai, China.

2.2. Preparation of adsorbent

A freshly prepared 20 mL ethanol suspension containing 2 wt% uniformly dispersed HNTs was mixed with 20 mL of ethanol solution containing 0.013 g of $ZrOCl_2{\cdot}8H_2O$ (final concentrations: 1 wt% HNTs and 1 mM Zr ions) (Ethanol's lower surface tension compared to water makes it more accessible to enter HNTs by capillary action, thus using ethanol as a solvent). The mixture was sonicated for 30 min, and then a vacuum environment was generated using a pump under magnetic stirring. The suspension was evacuated in a vacuum chamber for 30 min and then returned to atmospheric pressure. This vacuum-pressurization cycle was repeated three times to enhance the Zr ion loading efficiency [33]. After stirring ceased, the solid was separated and incubated with a 10% H_3PO_4 (*v*/v) solution for 24 h to facilitate the in situ growth of ZrP nanoparticles [7,34]. The resulting product was centrifuged at 10,000 rpm for 5 min, washed three times with ethanol and deionized water, and dried to obtain ZrP@HNTs. For comparison, ZrP nanocrystals deposited on the outer surface of HNTs (ZrP/HNTs) were also prepared. This was achieved by depositing ZrP onto the nanotube surfaces through the impregnation of HNTs with an aqueous $ZrOCl_2{\cdot}8H_2O$ solution (without vacuum assistance) [31], and the other steps follow the same procedure.

2.3. Characterization

The ZrP@HNTs and ZrP/HNTs were characterized with X-ray diffraction (D8 Advance diffractometer, Bruker, Germany), X-ray photoelectron spectroscopy (XPS, ESCALAB 250Xi, Thermo Fisher Scientific, USA), transmission electron microscope (TEM, JEM-F200, Japan) and automatic surface and porosity analyzer (BET, Micromeritics ASAP 2460, USA). A Nano-ZS instrument (Malvern Instruments Ltd., UK) was used to detect samples' zeta potentials. The Pb(II) concentrations were measured using an inductively coupled plasma-atomic emission spectrometer (ICP-OES, iCAP7400, ThermoFisher, USA) (see details in the supplementary texts).

2.4. Adsorption assay

Batch adsorption experiments were performed in 100 mL glass flasks under controlled temperature conditions. A detailed description is given in the supplementary texts.

2.5. Quartz crystal microbalance measurements (QCM-D)

The in-situ adsorption of lead ions on the gold sensors coated with ZrP@HNTs or ZrP/HNTs was monitored respectively by QCM-D (Q-Sense E4, Biolin Scientific) (see details in the supplementary texts).

2.6. DFT calculation

The binding energies (E_{ad}) for Pb(II) adsorption on optimized ZrP@HNTs or ZrP/HNTs species were calculated according to the following equation.

$$E_{ads} = E_{(adsorbent+adsorbed\ Pb(II))} - E_{(adsorbent)} - E_{(Pb(II))} \quad (1)$$

where $E_{(adsorbent+adsorbed\ Pb(II))}$ is the total energy, $E_{(adsorbent)}$ is the energy of the optimized ZrP@HNTs or ZrP/HNTs species, and $E_{(Pb(II))}$ is the energy of Pb(II).

2.7. Finite element simulation

To simulate the distribution of ions on different adsorbent surfaces, finite element simulations were conducted using COMSOL Multiphysics for the catalyst positioned both inside and outside the halloysite nanotubes. The modules used include diluted substance transfer, laminar flow, and electrostatic field (see details in the supplementary texts).

2.8. Atomic force microscopy (AFM) measurements

Using an AFM probe modified with phosphate groups, interaction forces were quantified in lead ion solutions (0.1 mM, 1 mM, and 10 mM). The adsorption behavior between phosphate and lead ion at varying concentrations was then characterized (see details in the supplementary texts).

3. Results and discussion

3.1. Synthesis and characterization of ZrP within HNTs' lumen

The preparation process of ZrP@HNTs and ZrP/HNTs were systematically expounded in Fig. 1. The synthesis of ZrP within the HNTs' lumen was accomplished using the modified solvent method in ethanol solutions. This process involves the hydrolysis of Zr^{4+} ions to form the precursor cations $[Zr(OH)_2{\bullet}4H_2O]_4^{8+}$, which adhere to the clay surface before being immersed in a phosphoric acid to facilitate the in situ growth of ZrP nanocrystals. Specifically, an ethanolic solution of $ZrOCl_2{\cdot}8H_2O$ is gradually introduced into an HNTs ethanol dispersion, and the Zr ions are vacuum-pumped into the HNT lumens [33]. Following complete adsorption and binding, Zr ions@HNTs are added to a phosphoric acid solution, where the in situ reaction proceeds for 24 h to produce ZrP@HNTs [7,34]. For comparison, ZrP/HNTs was prepared via a conventional impregnation method [31], where purified HNTs were directly mixed with an aqueous $ZrOCl_2{\cdot}8H_2O$ solution (without vacuum assistance), followed by phosphoric acid treatment under identical conditions. This approach primarily deposits ZrP on the outer surfaces of HNTs rather than within the lumen.

The transmission electron microscopy (TEM) clearly reveals that ZrP nanocrystals were dispersed on the inner surface of HNTs in ZrP@HNT (Fig. 2a) and on outer surface of HNTs in ZrP/HNT (Fig. 2c). For the ZrP@HNTs, it is observed that most ZrP nanocrystals are situated within the lumens of HNTs, where they are evenly distributed on the inner surfaces with minimal agglomeration. External surface of HNTs keep smooth, with nearly no ZrP nanocrystals present (TEM images of pristine halloysite nanotubes and pure zirconium phosphate nanocrystals are shown in Supplementary Fig. 1). The high-resolution transmission electron microscopy (HRTEM) image of the ZrP nanocrystals (Fig. 2a, c) displays distinct (−312) lattice fringes with an interplanar spacing of approximately 0.261–0.262 nm. These findings align with the structural data observed in the X-ray diffraction (XRD) spectra. The XRD diffraction peak intensities of ZrP nanocrystals in ZrP@HNTs and ZrP/HNTs were lower than those in the pure ZrP nanocrystals sample (Fig. 2g), indicating that the ZrP nanocrystals displayed reduced crystallinity and a smaller average crystallite size after interacting with HNTs. Additionally, the distribution and particle size of ZrP nanocrystals were examined using high-angle annular-dark field transmission electron microscopy (HAADF-STEM) coupled with energy-dispersive X-ray spectroscopy (EDX) elemental mapping. The findings reveal that ZrP nanocrystals were positioned inside the channels of HNTs in ZrP@HNTs (Fig. 2b and Supplementary Fig. 2a), whereas they exhibited a random dispersion on the exterior surface of HNTs in ZrP/HNTs (Fig. 2d and Supplementary Fig. 2b). Analysis of the size distribution revealed average particle sizes of 4.9 ± 0.2 nm for ZrP@HNTs and 9.5 ± 0.2 nm for ZrP/HNTs (Fig. 2e, f). BET measurements indicated specific surface areas of 57.9 $m^2\ g^{-1}$ for ZrP@HNTs and 30.4 $m^2\ g^{-1}$ for ZrP/HNTs (Supplementary Fig. 3). Notably, the surface area of ZrP@HNTs and ZrP/HNTs is larger than that of pristine HNTs. This enhancement in surface area can be ascribed to the deposition and dispersion of ZrP nanoparticles, which introduce additional mesopores and increase surface heterogeneity.

Zeta potential measurements indicated that the introduction of ZrP nanocrystals significantly enhanced the negative potential of HNTs, and the zeta potential of ZrP@HNTs and ZrP/HNTs was −48.6 mV and −45.8 mV, respectively (Fig. 2h). ZrP@HNTs integrated the positive charge of the inner wall of HNTs tube, therefore the zeta potential is slightly negative. This change would also be beneficial to the adsorption of heavy metals. The Zr content in both materials were nearly identical, as determined by acid digestion (1.45 wt% for ZrP@HNTs and 1.40 wt% for ZrP/HNTs, Supplementary Fig. 4).

The characteristic peak with the binding energy at 532.36 eV correspond to O 1 s electron of O^{2-} in ZrP@HNTs (Fig. 2i). At the same time, in the high-resolution XPS spectra of P 2p (Fig. 2j), a pair of characteristic peaks at 134.17 eV and 135.13 eV belong to the P 2p3/2 and P 2p1/2 electrons, respectively. The results showed that the electron binding energy of O 1 s and the P 2p electrons in ZrP@HNTs displays a certain degree of positive shift compared with ZrP/HNTs. Such a significant change in the zirconium phosphate was expected to have a substantial impact on its reactivity to heavy metals.

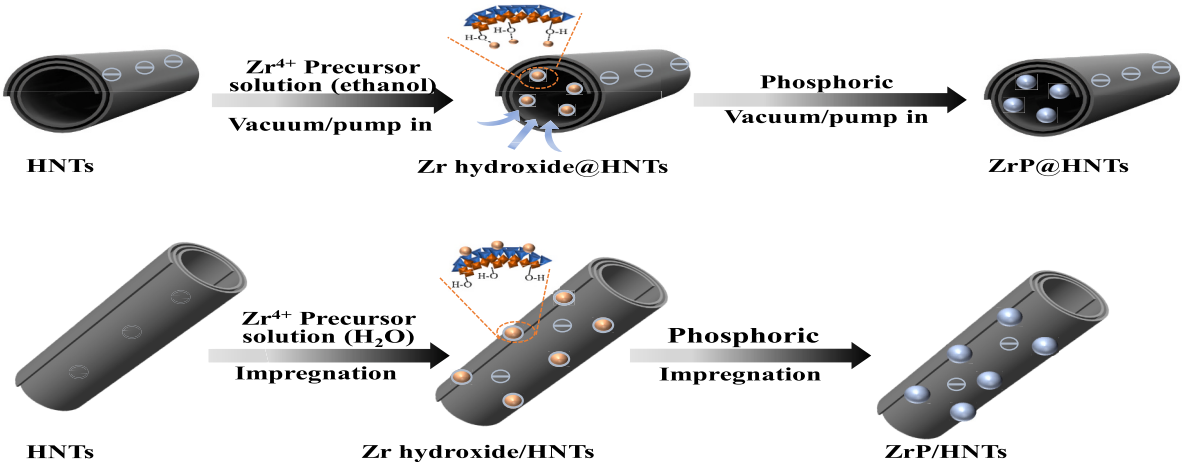

Fig. 1. Schematic illustration of the preparation strategy for ZrP@HNTs and ZrP/HNTs.

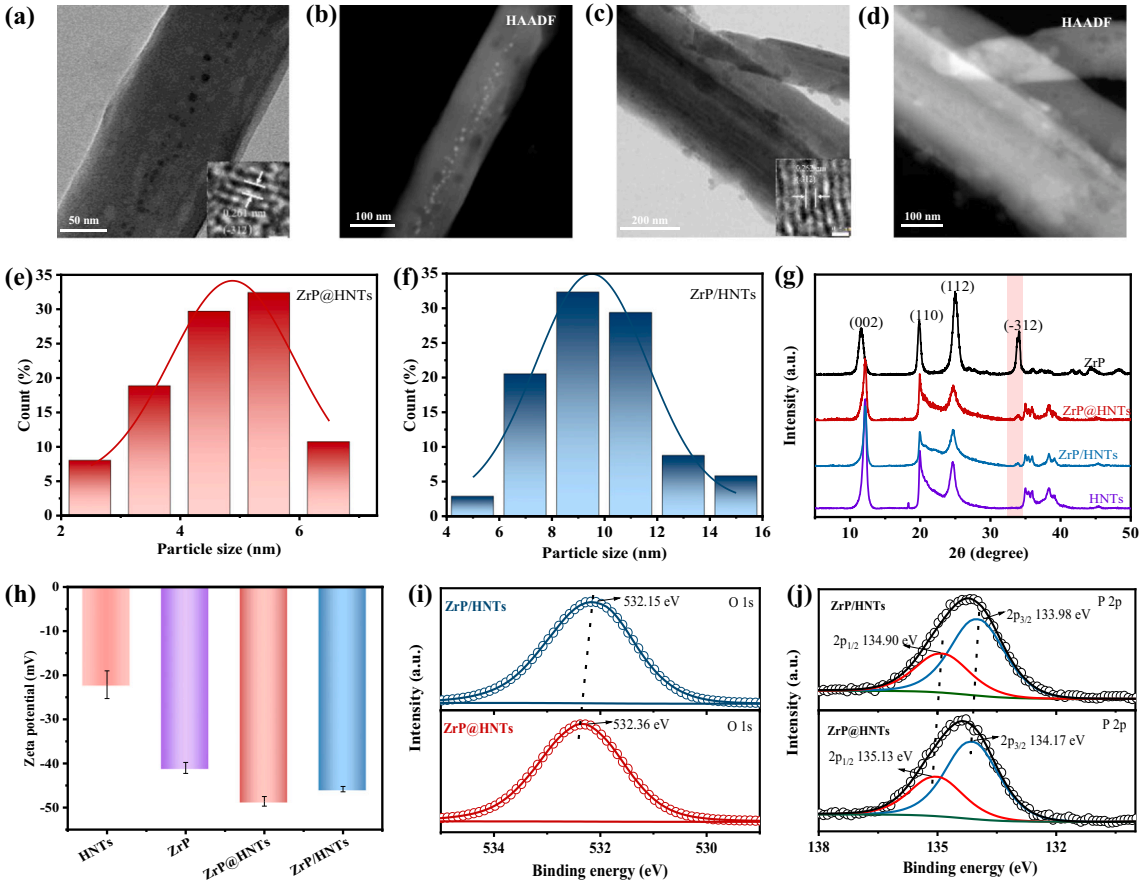

Fig. 2. Characterization of ZrP@HNTs and ZrP/HNTs. (a, c) TEM images of the ZrP@HNTs and ZrP/HNTs, respectively (inset: HRTEM images of ZrP nanocrystals). (b, d) HADDF-STEM images of ZrP@HNTs and ZrP/HNTs, respectively. (e, f) Particle size distributions of the ZrP nanocrystals in both ZrP@HNTs and ZrP/HNTs, respectively. (g) XRD patterns, (h) Zeta potentials (pH 7.0) of HNTs, ZrP@HNTs and ZrP/HNTs and ZrP. (i) O 1 s and (j) P 2p high-resolution XPS spectra of ZrP@HNTs and ZrP/HNTs.

3.2. Adsorption performance

To evaluate the adsorption performance of ZrP@HNTs for Pb(II) ions from aqueous solutions, pristine HNTs, ZrP, ZrP/HNTs, and ZrP@HNTs samples were immersed in a Pb(II) solution with initial concentration of 50 mg/L. After shaking for 10 h, the Pb(II)-loaded samples were separated to quantify the amount of adsorbed Pb(II). As shown in Fig. 3a, ZrP@HNTs exhibited higher adsorption capacities compared to HNTs, ZrP, and ZrP/HNTs. To further clarify the adsorption differences between ZrP@HNTs and ZrP/HNTs, quantitative adsorption tests were performed by quartz crystal microbalance (QCM-D) to directly monitor lead ion adsorption on ZrP@HNTs coated gold sensors and ZrP/HNTs coated gold sensors. As shown in Supplementary Fig. 5, after introducing the lead ion solution into the ZrP/HNTs coated gold sensor, it can be seen that the frequency is significantly reduced (~16 Hz), indicating that adsorption occurs on the surface of ZrP/HNTs. Compared with the ZrP/HNTs coated gold sensor, only a small amount of lead ions was adsorbed on the ZrP@HNTs coated gold sensor, indicating that the adsorption of lead ions by ZrP@HNTs mainly occurred in the lumen. Such a dramatic difference in adsorption reactivity inspired an investigation into the differences in the adsorption mechanisms of ZrP nanocrystals under nanoconfinement and nonconfinement.

The pH of the solution plays a critical role in modifying the surface functional groups of ZrP, thereby affecting its adsorption capacity. Thus, it is important to investigate how pH variations affect the adsorption of Pb(II) by the adsorbents. Fig. 3b shows the adsorption efficiency of ZrP@HNTs and ZrP/HNTs at pH 2–6. At pH 2–5, the results in Fig. 3b demonstrated that the adsorption efficiency of Pb(II) by ZrP/HNTs and ZrP@HNTs increased with pH increasing. At pH 5, ZrP/HNTs and ZrP@HNTs showed the highest removal efficiency of Pb(II), about 72.6% and 90.0%, respectively. From the overall trend change from pH 2 to 5, it can be seen that the effect of pH on the adsorption of lead ions by ZrP@HNTs is much smaller than that by ZrP/HNTs, which indicates that spatial nanoconfinement greatly reduces the effect of pH on the surface properties of ZrP and improves the acidic stability of ZrP. As the pH value increases further, the adsorption efficiency of Pb(II) by both ZrP/HNTs and ZrP@HNTs decreases. This is because Pb(II) exists entirely as Pb^{2+} at pH < 5. However, as the pH rises, the speciation of Pb (II) undergoes changes, which in turn impacts the ability of phosphate groups to adsorb Pb(II) [35].

The adsorption kinetics were examined. As shown in Fig. 3c, ZrP@HNTs exhibit a faster adsorption process compared to ZrP/HNTs, resulting in a higher adsorption rate constant with a strong correlation coefficient ($R^2 = 0.99$, Table S1) according to the pseudo-second-order kinetics model. The equilibrium adsorption isotherms of Pb(II) in ZrP@HNTs and ZrP/HNTs were derived experimentally using initial concentrations ranging from 10 to 400 mg/L, and were subsequently fitted using the Langmuir model (Fig. 3d), which provided a stronger correlation ($R^2 = 0.99$) compared to the Freundlich model ($R^2 = 0.88$, Supplementary Fig. 6). The maximum adsorption capacities of Pb(II) for ZrP@HNTs and ZrP/HNTs were 163.7 mg/g and 54.6 mg/g, respectively. This suggests that the confinement provided by halloysite nanotubes significantly enhances the Pb(II) adsorption capacity of ZrP nanocrystals.

Examining the selective adsorption of heavy metals by materials in the presence of competing mineral cations, such as Na(I) and Ca(II), in

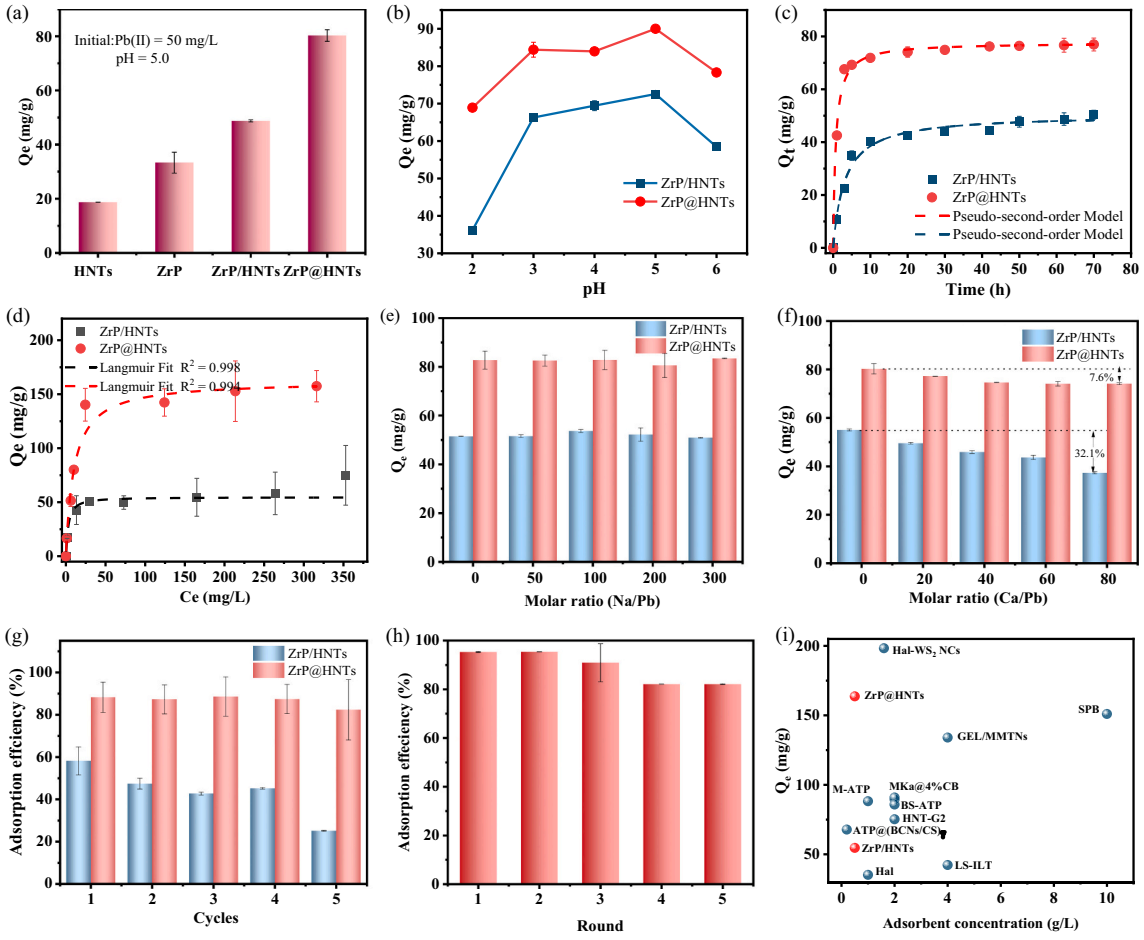

Fig. 3. (a) Adsorption capacity of HNTs, ZrP@HNTs and ZrP/HNTs and ZrP for Pb(II). (b) Effect of pH on the adsorption capacity. (c) Adsorption kinetics of Pb(II) with an initial concentration of 50 mg/L, fitted with a pseudo-second-order model. (d) Equilibrium Pb(II) adsorption capacity as a function of equilibrium Pb(II) concentration (Ce) fitted with the Langmuir model, (e, f) Effect of Na(I) and Ca(II) ions on adsorption of Pb(II) by the adsorbents. (g) Five cyclic adsorption-regeneration assays. (h) Multiple rounds of adsorption experiments of ZrP@HNTs in real mineral processing wastewater. (i) Comparison of maximum Pb(II) adsorption capacity and adsorbent dosage for various clay-based adsorbents.

real contaminated water is of vital practical significance. To explore the selective adsorption of Pb(II) in practical scenarios, we put the samples in Pb(II) solutions containing varying concentrations of Na or Ca ions as interfering agents. The results showed that the adsorption capacity of ZrP@HNTs and ZrP/HNTs for Pb(II) was almost unaffected when the molar ratio of Na(I)/Pb(II) was as high as 300 (Fig. 3e). This negligible interference effect can be attributed to the monovalent nature of Na(I) and its low affinity for phosphate functional groups. In contrast, phosphate functional groups prefer to bind to divalent or multivalent ions such as Pb(II) due to their stronger electrostatic interactions and coordination stability. When the molar ratio of Ca(II) to Pb(II) reached 80, the adsorption capacity of ZrP@HNTs and ZrP/HNTs for Pb(II) decreased by 7.6% and 32.1%, respectively (Fig. 3f). This suggests that ZrP nanocrystals in a confined system exhibit excellent selective adsorption capacity for heavy metals. These findings indicate that nanoconfinement enhances the inner-sphere coordination between ZrP@HNTs and heavy metals under strong competitive conditions, which leads to higher adsorption selectivity compared with the nonspecific electrostatic attraction between heavy metals [7,11,36].

Moreover, the ZrP@HNTs adsorbent can be efficiently regenerated through HCl washing and reused for multiple Pb(II) adsorption cycles. Remarkably, the adsorption capacity retained notably high (~82%) even after 5 cycles (Fig. 3g), demonstrating the adsorbent's long cycle life and further emphasizing the high stability of ZrP@HNTs. Additionally, the structural integrity was preserved, as confirmed by the identical XRD patterns of ZrP@HNTs before and after 5 cycles (Supplementary Fig. 7). Meanwhile, the dissolution of Zr during Pb(II) adsorption of ZrP@HNTs samples was evaluated (Supplementary Fig. 8). The lower dissolution of ZrP under nanoconfinement (leaching rate < 0.3 μg/L) indicates its beneficial effect on the stability of the nanocomposites in long-term applications.

To further evaluate the adsorption performance of ZrP@HNTs under practical conditions, real mining wastewater was used as the testing medium. As shown in Fig. 3h, the concentration of Pb(II) in the wastewater was reduced from 19.34 mg/L to 0.90 mg/L, corresponding to a removal efficiency of 95.29%. Furthermore, even after five successive additions of fresh wastewater into the system, ZrP@HNTs consistently maintained a Pb(II) removal efficiency above 80%, demonstrating its excellent adsorption capacity and operational stability in complex water matrices. In addition, the adsorption performance of ZrP@HNTs was compared with other clay-based adsorbents reported in recent years. As shown in Fig. 3i and Supplementary Table 2, ZrP@HNTs achieves relatively higher adsorption capacity with a lower dosage of adsorbent, highlighting its superior adsorption efficiency.

3.3. Adsorption mechanism investigation

To further explore the Pb(II) binding interactions in both confined and non-confined systems, additional characterizations were performed on ZrP@HNTs and ZrP/HNTs, providing deeper insights into the role of

nanoconfinement in enhancing adsorption efficiency. The ZrP@HNTs and ZrP/HNTs samples after adsorption of Pb(II) were characterized by XPS (Fig. 4a). When Pb(II) was adsorbed by ZrP@HNTs, the binding energy of Pb(II) 4f was lower, indicating that ZrP nanocrystals had a strong affinity for Pb(II) in the confined system. From P 2p peaks, after Pb(II) uptake, the peak shift of P 2p in ZrP@HNTs is about 2.4 times that of ZrP/HNTs (Fig. 4b). These results suggest that ZrP@HNTs interact much more strongly with Pb(II) than ZrP/HNTs.

The rationality of the regulation mechanism was further examined using DFT calculations. The adsorption energy (E_{ads}) calculations revealed that the confinement of ZrP nanocrystals within HNTs significantly enhanced the adsorption capacity for Pb(II) (Fig. 4c, d). This result indicates that Pb(II) is more strongly adsorbed into the HNTs nanotubes due to the additional interactions (e.g., electrostatic, van der Waals, or orbital interactions) from the confined space.

3.4. Mechanistic insight into adsorption enhancement under spatial nanoconfinement

To further study the mechanism of adsorption enhancement under spatial nanoconfinement, we conducted research from the aspects of reactant enrichment, mass transfer effect, and interaction mechanism at the nano-scale.

3.4.1. Reactant enrichment effect

Reactant enrichment is regarded as a key feature of the nanoconfinement effect within the microenvironment of nanoreactors. In hollow tubular nanostructures, the internal void space creates a confined region with concave interfaces that promote the accumulation of reactant molecules. By incorporating active sites within this confined space, the local concentration of reactants is significantly increased, leading to an accelerated reaction rate [37]. Consequently, the impact of the reactant enrichment effect was thoroughly studied under spatial nanoconfinement. The initial nucleation and early growth of Pb(II) with different concentrations on phosphate monolayer (representing phosphate adsorbed groups on ZrP nanocrystals) modified substrates were observed by in situ AFM (Fig. 5) [38–40]. AFM results showed that the reaction rate of Pb(II) and phosphate functional groups is proportional to the concentration of Pb(II). The surface roughness of the substrate after Pb(II) reaction at different reaction times is shown in Fig. 5. According to the variation of roughness, the nucleation and growth rate of high-concentration Pb(II) on the substrate surface is much faster than that of low-concentration Pb(II). In addition, due to spatial confinement, the pH change of the solution in the confinement space will be more significant than that of the bulk solution, and the pH will affect the surface properties of the functional groups, thus affecting the adsorption of heavy metal ions by the material. The results showed (Fig. 3b) that the effect of pH on ZrP@HNTs is much smaller than that on ZrP/HNTs, whereas for ZrP@HNTs, the adsorption of Pb(II) remains high in the range of pH 2–5, which implies that there are other important factors for adsorption enhancement under the spatial confinement.

3.4.2. Mass transfer effect

In bulk phase solutions, mass transfer depends mainly on molecular diffusion, following Fick's rule. In confined space, because the space is very small, the movement of molecules in the pore may be limited, causing them to be enriched in the confined space [15,16]. According to the COMSOL simulation (Fig. 6), the localized action of nanotubes promoted the local enrichment of lead ion concentration in the tube, and the concentration of Pb(II) on the near-surface was basically consistent with that in the center of the tube. But outside the tube, due to its poor mass transfer efficiency, an obvious concentration gradient can be observed. Therefore, there will also be a thicker diffusion layer in the outer space [41,42]. As can be seen from the change of Pb(II) concentration within 100 μs (Supplementary Fig. 9), ZrP@HNTs mass transfer is accelerated due to the confinement effect of nanotubes, and Pb(II) quickly reaches saturation concentration on the surface of ZrP [43]. According to Fick's law, reducing the thickness of the diffusion layer can significantly enhance the mass transfer of reactants, enhance the collision between adsorbent and adsorbent, and improve the adsorption efficiency. The change of diffusion layer and the change of local concentration of reactants will also cause the change of intermolecular force of reactants.

3.4.3. The interaction mechanism

AFM has been widely used to measure surface interaction mechanisms at the nanoscale [44–46]. Chemical force microscopy (CFM), an AFM-based technique, directly measures interaction forces between self-

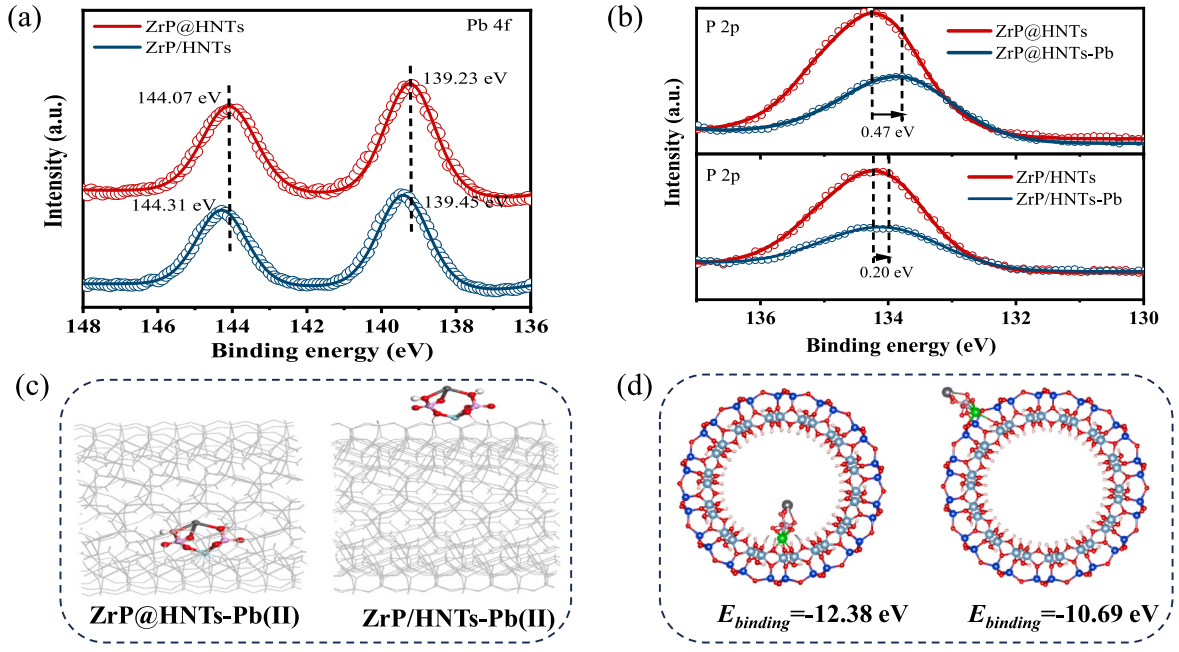

Fig. 4. (a) XPS Pb 4f spectra of Pb(II)-loaded adsorbents, and (b) XPS P 2p spectra of the adsorbents before and after Pb(II) uptake. Theoretical calculations. (c) Optimized structures of ZrP@HNTs and ZrP/HNTs after adsorption of ions. (d) The adsorption energy (Eads) of Pb(II) on ZrP@HNTs and ZrP/HNTs.

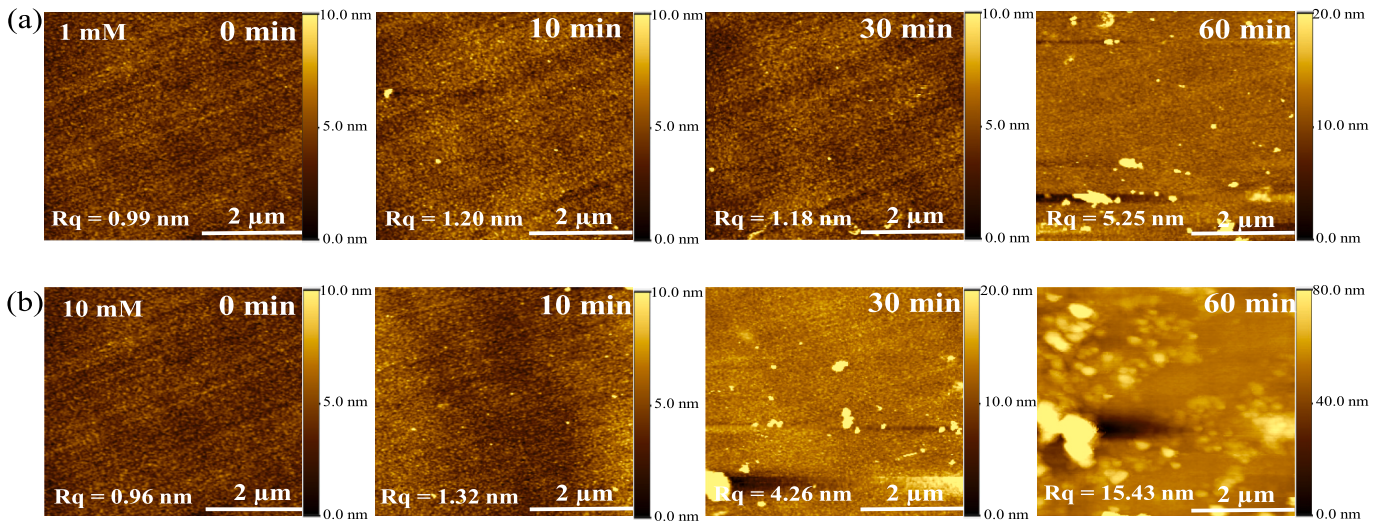

Fig. 5. In situ AFM images of the initial nucleation and early growth of (a) 1 mM Pb(II) and (b) 10 mM Pb(II) on the substrate.

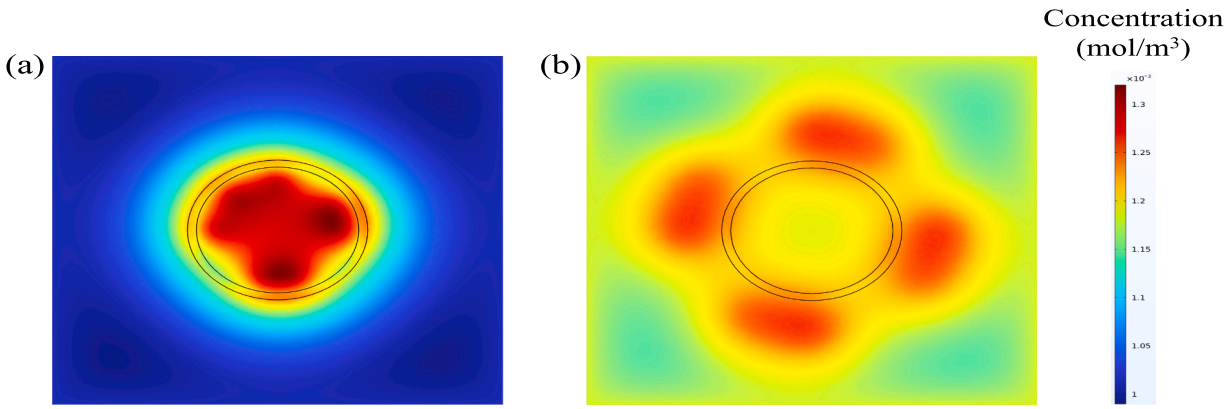

Fig. 6. Visualization of Pb (II) distribution on cross sections (top) of (a) ZrP@HNTs and (b) ZrP/HNTs.

assembled monolayers (SAM) with specific terminal groups, such as -CH_3, -OH, and -COOH [47]. To investigate changes in the interaction force and binding strength between reactants within confined spaces, we utilized H_2PO_4-SAM molecules to model the phosphate groups on ZrP nanocrystal. Different concentrations of lead ions were employed to simulate the enrichment of ion concentrations in both nonconfined and confined structures [48]. CFM was used to quantitatively measure the interaction force and adhesion energy between lead ions of different concentrations and adsorbed functional groups at the nanoscale.

Fig. 7 (a-c) shows the interaction force between the AFM tip functionalized with H_2PO_4-SAM and the coated substrate in solutions with different Pb(II) concentrations (pH = 5.0 ± 0.1). The force measurement results (empty symbols) were fitted by DLVO theory. The difference between the measured data and the theoretical fit is mainly due to the influence of surface roughness and possible hydration. As shown in Fig. 7, the phosphate group exhibit an attraction from ~3 nm with 0.1 mM Pb(II), ~ 7 nm with 1 mM Pb(II) and ~ 11 nm with 10 mM Pb(II) [49–51]. This indicates that as the ion concentration increases, the double electrical layer is compressed, and the functional groups and ions generate attraction at a farther range, thereby improving the adsorption efficiency.

The adherence F_{adh}/R histogram measured during the separation process and the fitted Gaussian distribution (solid curve) between phosphate-Pb(II)-phosphate in solutions with different Pb(II) concentrations at pH 5.0 ± 0.1 are shown in Fig. 7 (d-f). The calculated average normalized adhesion forces were 27.24 ± 0.93 mN·m^{-1}, 47.32 ± 0.5 mN·m^{-1} and 67.86 ± 1.67 mN·m^{-1} at 0.1 mM, 1 mM and 10 mM Pb(II) solutions, respectively. Obviously, as the ion concentration increases, the average adhesion force increases significantly [52]. Using the Derjaguin-Muller-Toporov (DMT) model $W_{adh} = -F_{adh}/2\pi R$ to correlate the measured adhesion F_{adh}/R to the adhesion energy per unit area W_{adh}, the average adhesion energy was calculated to be ~4.34 mJ·m^{-2} for 0.1 mM Pb(II), ~ 7.54 mJ·m^{-2} for 1 mM Pb(II) and ~ 10.81 mJ·m^{-2} for 10 mM Pb(II). Adhesion energy can be provided by various interactions, including hydrogen bonding, electrostatic forces, and coordination effects. The increase in ion concentration leads to an enhanced electrostatic shielding effect, which weakens the electrostatic interaction between functional group molecules. However, in the case of coordination between functional groups and metal ions, higher ion concentrations can strengthen the interaction by facilitating the formation of more stable coordination complexes [53]. Therefore, under high concentration conditions, the selective adsorption ability of functional groups to ions will also increase.

In general, the excellent performance of ZrP@HNTs can be attributed to the optimization of material structure and the regulation of interaction force (Fig. 8). Specifically, the adsorbent prepared in the nanoconfinement space is not only smaller in size and more evenly distributed, but also exposes more active sites, thereby significantly improving the adsorption capacity. Nanoconfinement can help maintain the structural stability of materials and prevent structural changes or leaching during the adsorption process, thereby maintaining efficient adsorption capacity. Meanwhile, the nanoconfinement can promote the

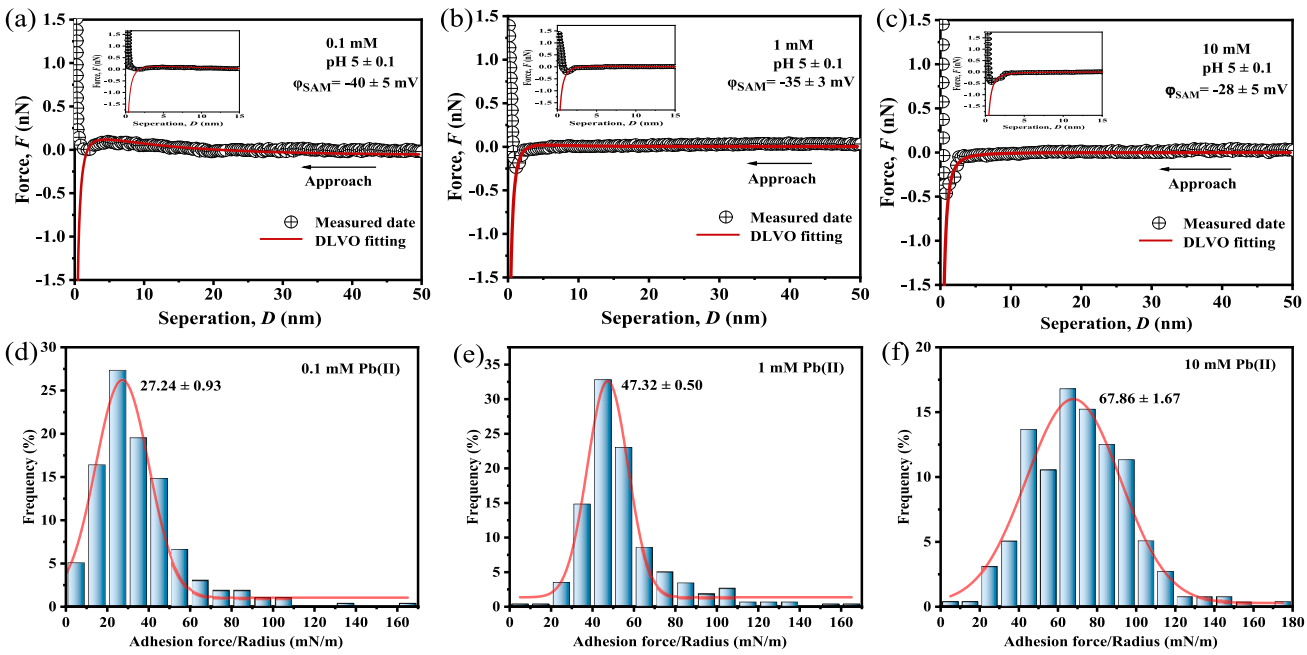

Fig. 7. Typical forced-separation curves between the coated AFM probe and surface at pH ~ 5.0 (a) 0.1 mM , (b) 1 mM and (c) 10 Mm Pb(II) (Experiment results are shown in open symbols and theoretical calculations are shown in red curves, illustration: Zoom view at short-term separation). The histogram of measured adhesion force Fadh/R with the fitted Gaussian distribution between the coated AFM probe and surface at pH ~ 5.0 (d) 0.1 mM, (e) 1 mM and (f) 10 Mm Pb(II).

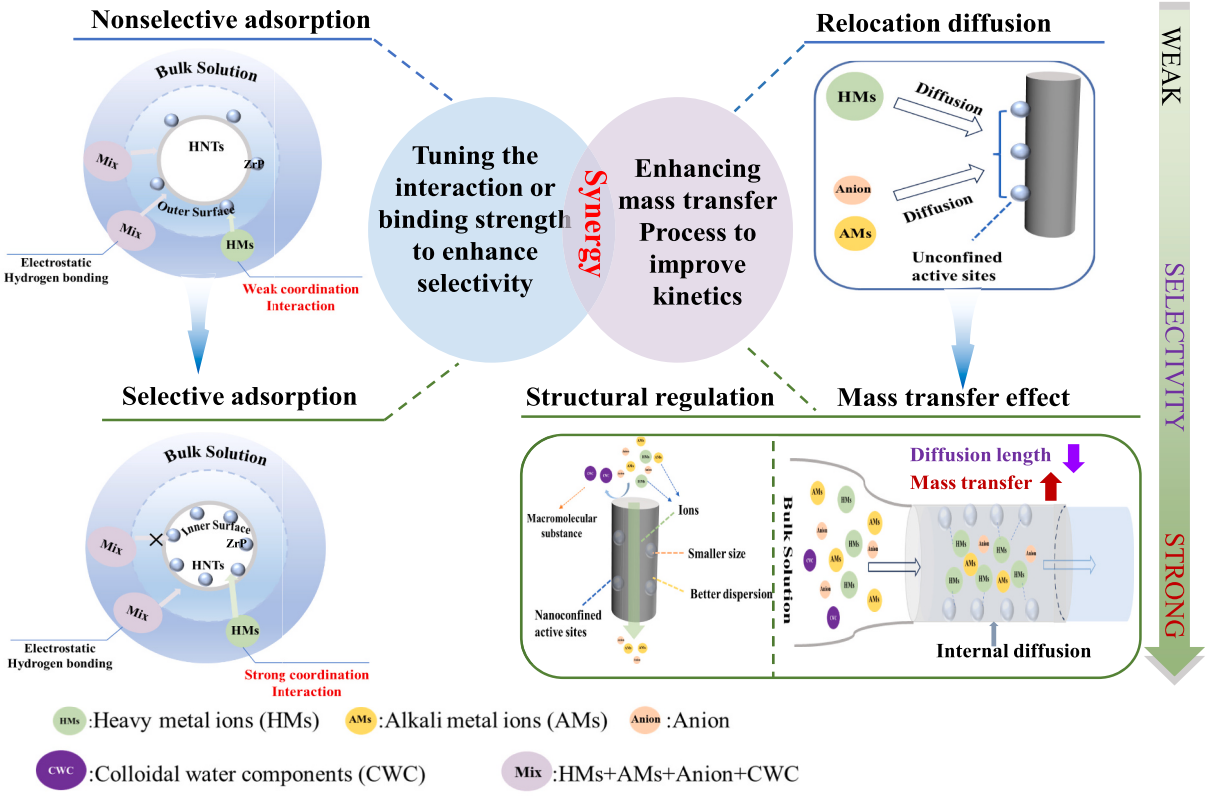

Fig. 8. Overview of nanoconfinement strategies for enhanced adsorption.

local enrichment of reactants, accelerate interfacial reactions and adsorption processes, and further strengthen the interaction between the adsorbent and heavy metal ions.

4. Conclusion

In summary, this work demonstrates that nanoconfinement can significantly enhance heavy metal adsorbent performance. By leveraging the intrinsic tubular lumen of halloysite nanotubes (HNTs) as

a confined space, zirconium phosphate (ZrP) nanocrystals were grown in situ to form a nanoconfined structure (ZrP@HNTs) with precise control over crystallite size (4.9 nm) and uniform dispersion. Compared to ZrP nanocrystals on the outer surface of HNTs (ZrP/HNTs), ZrP@HNTs exhibited a threefold increase in Pb(II) adsorption capacity and maintained high stability, retaining over 80% of its adsorption capacity after five cycles. Finite element simulations confirmed that the nanoconfined HNT lumen effectively enriches Pb(II) and reduces the diffusion layer thickness, thereby accelerating adsorption kinetics. Based on the finite element simulations results, adsorption environments for ZrP@HNTs and ZrP/HNTs were modeled using high and low concentrations of Pb (II) solutions, respectively. Atomic force microscopy analysis measured the variation in interaction forces between Pb(II) at concentrations ranging from 0.1 mM to 10 mM and phosphate groups on ZrP, with adhesion energy increasing from 4.34 $mJ{\cdot}m^{-2}$ to 10.81 $mJ{\cdot}m^{-2}$. This directly quantifies the contribution of the nanoconfined space to the enhancement of adsorption. This work proves the effectiveness of nanoconfinement in optimizing adsorbent performance and provides a powerful strategy for the design of sustainable water treatment technologies.

CRediT authorship contribution statement

Rong Yang: Writing – review & editing, Writing – original draft, Data curation, Conceptualization. **Di Meng:** Visualization, Investigation. **Xinyao Zhang:** Investigation, Data curation. **Weixuan Zhao:** Investigation, Formal analysis. **Xuanjie Huang:** Formal analysis, Data curation. **Zulin Wang:** Formal analysis, Data curation, Conceptualization. **Bo Ma:** Formal analysis, Data curation. **Jun Yao:** Formal analysis, Data curation. **Wenjihao Hu:** Writing – review & editing, Supervision, Conceptualization.

Declaration of competing interest

The authors declare that they have no known competing financial interests or personal relationships that could have appeared to influence the work reported in this paper.

Acknowledgments

Thanks for the support of the National Key Research and Development Program of China (2023YFC3707602), the National Natural Science Foundation Youth project (52104284), the National Natural Science Foundation of China (5210041330), and postgraduate Scientific Research Innovation Project of Central South University (512340028).

Appendix A. Supplementary data

Supplementary data to this article can be found online at https://doi.org/10.1016/j.cej.2025.165613.

Data availability

Data will be made available on request.

References

[1] G. Xiao, R. Li, D. Zhu, M. Vakili, X. Zhu, X. Liu, S. Zhou, W. Wang, Adsorption of Pb (II) on covalent organic frameworks: overlooked sorption sites formed in the post-synthetic modification process, Colloids Surfaces A Physicochem. Eng. Asp. 681 (2024) 132791.
[2] P.A. Atmianlu, R. Badpa, V. Aghabalaei, M. Baghdadi, A review on the various beds used for immobilization of nanoparticles: overcoming the barrier to nanoparticle applications in water and wastewater treatment, J. Environ. Chem. Eng. 9 (2021) 106514.
[3] J. Qian, X. Gao, B. Pan, Nanoconfinement-mediated water treatment: from fundamental to application, Environ. Sci. Technol. 54 (2020) 8509–8526.
[4] Y. Du, X. Wang, G. Nie, L. Xu, Y. Hu, Enhanced phosphate removal by using La-Zr binary metal oxide nanoparticles confined in millimeter-sized anion exchanger, J. Colloid Interface Sci. 580 (2020) 234–244.
[5] K. Liu, D. Zhao, Z. Hu, Y. Xiao, C. He, F. Jiang, N. Zhao, C. Zhao, W. Zhang, R. Qiu, The adsorption and reduction of anionic Cr(VI) in groundwater by novel iron carbide loaded on N-doped carbon nanotubes: effects of Fe-confinement, Chem. Eng. J. 452 (2023) 139357.
[6] L. Xing, M. Li, T. Qi, L. Mao, Z. Hu, E. Zhang, G.-P. Hao, B. Mao, L. Wang, Construction of confined bifunctional 2D material for efficient sulfur resource recovery and Hg^{2+} adsorption in desulfurization, Environ. Sci. Technol. 56 (2022) 4531–4541.
[7] X. Zhang, J. Shen, S. Pan, J. Qian, B. Pan, Metastable zirconium phosphate under nanoconfinement with superior adsorption capability for water treatment, Adv. Funct. Mater. 30 (2020) 1909014.
[8] G. Shen, L. Pan, R. Zhang, S. Sun, F. Hou, X. Zhang, J.J. Zou, Low-spin-state hematite with superior adsorption of anionic contaminations for water purification, Adv. Mater. 32 (2020) 1905988.
[9] B.D. Hamilton, J.-M. Ha, M.A. Hillmyer, M.D. Ward, Manipulating crystal growth and polymorphism by confinement in nanoscale crystallization chambers, Acc. Chem. Res. 45 (2012) 414–423.
[10] A.B. Grommet, M. Feller, R. Klajn, Chemical reactivity under nanoconfinement, Nat. Nanotechnol. 15 (2020) 256–271.
[11] X. Wang, Z. Jiang, J. Qian, W. Fu, B. Pan, Structure evolution of Iron (Hydr) oxides under Nanoconfinement and its implication for water treatment, Environ. Sci. Technol. 58 (2023) 826–835.
[12] D. Wang, S. Li, C. Wu, T. Li, Surface-seal encapsulation of a homogeneous catalyst in a mesoporous metal–organic framework, J. Am. Chem. Soc. 144 (2022) 685–689.
[13] F. Ma, D. Zhang, T. Huang, N. Zhang, Y. Wang, Ultrasonication-assisted deposition of graphene oxide on electrospun poly (vinylidene fluoride) membrane and the adsorption behavior, Chem. Eng. J. 358 (2019) 1065–1073.
[14] C. Wu, M. Xia, W. Jiang, H. Liu, S. Liu, G. Lyu, S. Wu, Y. Ni, Y. Liu, Hollow-structured resin Nanoreactor with high-loading of Ag nanoparticles and void-confinement effect for efficient catalytic hydrogenation, Compos. Part B Eng. 296 (2025) 112267. Elsevier.
[15] W. Chen, X. Pan, M.G. Willinger, D.S. Su, X. Bao, Facile autoreduction of iron oxide/carbon nanotube encapsulates, J. Am. Chem. Soc. 128 (2006) 3136–3137.
[16] D. Yao, Y. Wang, K. Hassan-Legault, A. Li, Y. Zhao, J. Lv, S. Huang, X. Ma, Balancing effect between adsorption and diffusion on catalytic performance inside hollow nanostructured catalyst, ACS Catal. 9 (2019) 2969–2976.
[17] M. Tang, J. Wan, Y. Wang, G. Ye, Z. Yan, Y. Ma, J. Sun, Overlooked role of void-nanoconfined effect in emerging pollutant degradation: modulating the electronic structure of active sites to accelerate catalytic oxidation, Water Res. 249 (2024) 120950.
[18] Z. Liu, J. Liu, H. Li, P. Xia, R. Zhu, W. Bi, Q. Liu, X. Zhang, P. Liang, Regulation of metal utilization ratio and active sites of nickel phyllosilicates for enhanced CO2 methanation, Chem. Eng. J. 496 (2024) 154111.
[19] W. Zhou, X. Ma, Advances in understanding the active sites of cu catalysts in glycerol hydrogenolysis to 1, 2-propanediol, Catal. Rev. 66 (2024) 1288–1315.
[20] Z. Zhou, F. Yu, J. Ma, Nanoconfinement Engineering for Enchanced Adsorption of Carbon Materials, Metal–Organic Frameworks, Mesoporous Silica, MXenes and Porous Organic Polymers: A Review, Springer International Publishing, 2022.
[21] L. Lisuzzo, G. Cavallaro, S. Milioto, G. Lazzara, Halloysite nanotubes as nanoreactors for heterogeneous micellar catalysis, J. Colloid Interface Sci. 608 (2022) 424–434.
[22] G. Cavallaro, G. Lazzara, S. Milioto, Nanocomposites based on halloysite nanotubes and sulphated galactan from red seaweed Gloiopeltis: properties and delivery capacity of sodium diclofenac, Int. J. Biol. Macromol. 234 (2023) 123645.
[23] Y. Feng, X. Luo, Z. Li, X. Fan, Y. Wang, R.-R. He, M. Liu, A ferroptosis-targeting ceria anchored halloysite as orally drug delivery system for radiation colitis therapy, Nat. Commun. 14 (2023) 5083.
[24] P. Zhao, J. Hu, Y. Feng, F. Wu, C. Tan, X. Chen, M. Liu, Cu_3-xP nanocrystals filled halloysite nanotubes for chemodynamic therapy of breast cancer, J. Colloid Interface Sci. 655 (2024) 736–747.
[25] T. Rostamzadeh, M.S. Islam Khan, K. Riche', Y.M. Lvov, A.V. Stavitskaya, J. B. Wiley, Rapid and controlled in situ growth of noble metal nanostructures within halloysite clay nanotubes, Langmuir 33 (2017) 13051–13059.
[26] A. Glotov, A. Vutolkina, A. Pimerzin, V. Vinokurov, Y. Lvov, Clay nanotube-metal core/shell catalysts for hydroprocesses, Chem. Soc. Rev. 50 (2021) 9240–9277.
[27] T. Takei, K. Aoyama, S. Yanagida, N. Kumada, Y. Nakajima, Circumstances of La, Eu, Dy, and Yb cations intercalated via ion exchange in γ-zirconium phosphate, Inorg. Chem. 57 (2018) 13097–13103.
[28] D. Gui, X. Dai, Z. Tao, T. Zheng, X. Wang, M.A. Silver, J. Shu, L. Chen, Y. Wang, T. Zhang, Others, unique proton transportation pathway in a robust inorganic coordination polymer leading to intrinsically high and sustainable anhydrous proton conductivity, J. Am. Chem. Soc. 140 (2018) 6146–6155.
[29] S.J. Tesh, T.B. Scott, Nano-composites for water remediation: a review, Adv. Mater. 26 (2014) 6056–6068.
[30] Y.X. Lee, F. Ahmad, S. Kabir, P.J. Masset, E. Onate, G.H. Yeoh, Synergistic effects of tubular halloysite clay and zirconium phosphate on thermal behavior of intumescent coating for structural steel, J. Mater. Res. Technol. 18 (2022) 4456–4469.
[31] B. Sriram, M.A. Ghanem, S.F. Wang, V.A. Sherlin, M. George, Designing of highly active hexagonal α-zirconium phosphate nanoparticles decorated halloysite nanotube composite for voltammetry sensing of azomycin drug, Chem. Eng. J. 509 (2025) 161220.

[32] L. Li, J. Zhao, Y. Zhang, Y. Wang, Y. Wang, B. Su, F. Li, L. Shi, P. Li, Z. Zhang, X. Zhang, J. Mu, Y. Dong, Construction of proton exchange membrane with high proton conductivity based on 3D self-assembly structures as multiple proton transport channels, Int. J. Hydrog. Energy 97 (2025) 419–430.
[33] Y. Feng, D. Zhang, X. Chen, C. Zhou, M. Liu, Confined-synthesis of ceria in tubular Nanoclays for UV protection and anti-biofilm application, Adv. Funct. Mater. 34 (2024) 1–14.
[34] M. Wang, M. Fu, J. Li, Y. Niu, Q. Zhang, Q. Sun, New insight into polystyrene ion exchange resin for efficient cesium sequestration: the synergistic role of confined zirconium phosphate nanocrystalline, Chin. Chem. Lett. 35 (2024) 108442.
[35] S. Pan, J. Shen, Z. Deng, X. Zhang, B. Pan, Metastable nano-zirconium phosphate inside gel-type ion exchanger for enhanced removal of heavy metals, J. Hazard. Mater. 423 (2022) 127158.
[36] X. Zhang, C. Cheng, J. Qian, Z. Lu, S. Pan, B. Pan, Highly efficient water decontamination by using sub-10 nm FeOOH confined within millimeter-sized mesoporous polystyrene beads, Environ. Sci. Technol. 51 (2017) 9210–9218.
[37] G. Prieto, H. Tüysüz, N. Duyckaerts, J. Knossalla, G.H. Wang, F. Schüth, Hollow nano-and microstructures as catalysts, Chem. Rev. 116 (2016) 14056–14119.
[38] S. Zhang, L. Cheng, X. Zuo, D. Cai, K. Tong, Y. Hu, J. Ni, (Fe, Cr)$(OH)_3$ Coprecipitation in solution and on soil: roles of surface functional groups and solution pH, Environ. Sci. Technol. 57 (2023) 7516–7525.
[39] M. Yu, Z. Gan, W. Zhang, C. Yang, Y. Zhang, A. Tang, X. Dong, H. Yang, Differential adsorption of dissolved organic matter and phosphorus on clay mineral in water-sediment system, Environ. Sci. Technol. 58 (2024) 2078–2088.
[40] X. Zhou, B. Wen, Y. Cai, X. Chen, L. Li, Q. Zhao, S.L. Chou, F. Li, Interfacial engineering for oriented crystal growth toward dendrite-free Zn anode for aqueous zinc metal battery, Angew. Chem. Int. Ed. 63 (2024) e202402342.
[41] H. Xin, H. Wang, W. Zhang, Y. Chen, Q. Ji, G. Zhang, H. Liu, A.D. Taylor, J. Qu, In operando visualization and dynamic manipulation of electrochemical processes at the electrode–solution interface, Angew. Chem. Int. Ed. 61 (2022) e202206236.
[42] Y. Kang, Z. Gu, B. Ma, W. Zhang, J. Sun, X. Huang, C. Hu, W. Choi, J. Qu, Unveiling the spatially confined oxidation processes in reactive electrochemical membranes, Nat. Commun. 14 (2023) 6590.
[43] S. Liang, L.J. Zheng, L.N. Song, X.X. Wang, W.B. Tu, J.J. Xu, Accelerated Confined Mass Transfer of MoS_2 1D Nanotube in Photo-Assisted Metal–Air Batteries, Adv. Mater. 36 (2024) 2307790.
[44] Q. Lu, Z. Wang, S. Zhang, J. Wang, X. Mao, L. Xie, Q. Liu, H. Zeng, Molecular interaction mechanism for humic acids fouling resistance on charged, zwitterion-like and zwitterionic surfaces, J. Colloid Interface Sci. 666 (2024) 393–402.
[45] J. Peng, D. Cao, Z. He, J. Guo, P. Hapala, R. Ma, B. Cheng, J. Chen, W.J. Xie, X.Z. Li, Others, the effect of hydration number on the interfacial transport of sodium ions, Nature 557 (2018) 701–705.
[46] J. Liu, X. Cui, L. Xie, J. Huang, L. Zhang, J. Liu, X. Wang, J. Wang, H. Zeng, Probing effects of molecular-level heterogeneity of surface hydrophobicity on hydrophobic interactions in air/water/solid systems, J. Colloid Interface Sci. 557 (2019) 438–449.
[47] L. Xie, J. Wang, C. Shi, X. Cui, J. Huang, H. Zhang, Q. Liu, Q. Liu, H. Zeng, Mapping the nanoscale heterogeneity of surface hydrophobicity on the sphalerite mineral, J. Phys. Chem. C 121 (2017) 5620–5628.
[48] M. Yu, Y. Hua, M.T. Sarwar, H. Yang, Nanoscale interactions of humic acid and minerals reveal mechanisms of carbon protection in soil, Environ. Sci. Technol. 57 (2022) 286–296.
[49] L. Xie, Q. Lu, X. Mao, J. Wang, L. Han, J. Hu, Q. Lu, Y. Wang, H. Zeng, Probing the intermolecular interaction mechanisms between humic acid and different substrates with implications for its adsorption and removal in water treatment, Water Res. 176 (2020) 115766.
[50] Q. Lu, J. Wang, Z. Wang, L. Xie, Q. Liu, H. Zeng, Molecular insights into the interaction mechanism underlying the aggregation of humic acid and its adsorption on clay minerals, Environ. Sci. Technol. 57 (2023) 9032–9042.
[51] W. Hu, M. Tian, J. Cao, L. Xie, L. Gong, W. Sun, Z. Gao, H. Zeng, Probing the interaction mechanism between benzohydroxamic acid and mineral surface in the presence of Pb^{2+} ions by AFM force measurements and first-principles calculations, Langmuir 36 (2020) 8199–8208.
[52] W. Hu, L. Xie, C. Zhang, J. Wang, C. Qiao, S. Li, J. Chen, Z. Zhao, H. Zeng, Demystifying constructive strategies on designing functionalized lamellar Nb_2CT_x nanosheet membrane architectures under confined space, J. Mater. Chem. A 10 (2022) 4200–4208.
[53] C. Tian, J. Tu, P. Qiu, S. Wang, H. Song, Y. Xu, X. Yan, Z. Lin, L. Chai, Ultrastrong anion affinity of anionic clay induced by its inherent nanoconfinement, Environ. Sci. Technol. 55 (2020) 930–940.